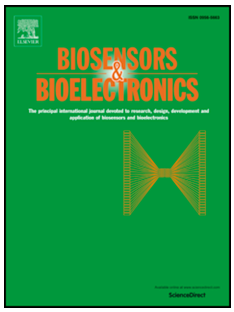

Modulation of oligonucleotide-binding dynamics on WS_2 nanosheet interfaces for detection of Alzheimer's disease biomarkers

Hye-In Kim, DaBin Yim, Su-Ji Jeon, Tae-Woog Kang, In-Jun Hwang, Sin Lee, Jin-Kyung Yang, Jong-Min Ju, Yoonhee So, Jong-Ho Kim

PII: S0956-5663(20)30395-X

DOI: https://doi.org/10.1016/j.bios.2020.112401

Reference: BIOS 112401

To appear in: *Biosensors and Bioelectronics*

Received Date: 30 March 2020

Revised Date: 8 June 2020

Accepted Date: 18 June 2020

Please cite this article as: Kim, H.-I., Yim, D., Jeon, S.-J., Kang, T.-W., Hwang, I.-J., Lee, S., Yang, J.-K., Ju, J.-M., So, Y., Kim, J.-H., Modulation of oligonucleotide-binding dynamics on WS_2 nanosheet interfaces for detection of Alzheimer's disease biomarkers, *Biosensors and Bioelectronics* (2020), doi: https://doi.org/10.1016/j.bios.2020.112401.

Modulation of Oligonucleotide-Binding Dynamics on WS_2 Nanosheet Interfaces for Detection of Alzheimer's Disease Biomarkers

*Hye-In Kim, DaBin Yim, Su-Ji Jeon, Tae-Woog Kang, In-Jun Hwang, Sin Lee, Jin-Kyung Yang, Jong-Min Ju, Yoonhee So, and Jong-Ho Kim**

Department of Chemical Engineering, Hanyang University, Ansan 426-791, Republic of Korea

*To whom correspondence should be addressed: kjh75@hanyang.ac.kr

Abstract

Non-covalent adsorption and desorption of oligonucleotides on two-dimensional nanosheets are widely employed to design nanobiosensors for the rapid optical detection of targets. A precise control over the weak interactions between nanosheet interfaces and oligonucleotides is crucial for a high-sensing performance. Herein, the interface of ultrathin WS_2 nanosheets used as a fluorescence quencher was engineered by four different dextran polymers in an aqueous solution to control the adsorption kinetics and thermodynamics of the DNA probe. The WS_2 nanosheets, functionalized by the carboxyl group-bearing dextran (CM-dex-WS_2) or the trimethylammonium-modified dextran (TMA-dex-WS_2), exhibited 3.6-fold faster adsorption rates of the fluorescein-labeled DNA probe (FAM-DNA), which led to the effective fluorescence quenching of FAM, compared to the nanosheets functionalized with pristine dextran (dex-WS_2) or the hydrophobic phenoxy groups-bearing dextran (PhO-dex-WS_2). Isothermal titration calorimetry measurements showed that the adsorption strength of FAM-DNA for CM-dex-WS_2 was one order of magnitude greater than its hybridization energy for a target microRNA (miR-29a) that is well-known as an Alzheimer's disease (AD) biomarker, leading to the unfavorable desorption of the DNA probe from the surface. In contrast, TMA-dex-WS_2 exhibited the proper adsorption strength of FAM-DNA, which was lower than its hybridization energy for miR-29a, leading to its favorable desorption from the nanosheet surface along with the noticeable restoration of the quenched fluorescence after its hybridization with miR-29a. Finally, the interface modulation of WS_2 nanosheets allowed the selective and sensitive recognition of miR-29a against non-complementary RNA and single base-mismatched RNA in human serum via increases in target-specific fluorescence.

Keywords: Alzheimer's disease, interface engineering, microRNA detection, optical biosensor, and WS_2 nanosheet

1. Introduction

MicroRNAs (miRNAs) are a group of short and functional non-coding RNAs that regulate the expression of target mRNAs via their degradation and translation repression (Bartel 2004). The aberrant function of the regulatory miRNAs has been found to be associated with various diseases (Ikeda et al. 2007; Mitchell et al. 2008). In addition, several miRNAs have been known to be expressed in the human brain (Sempere et al. 2004), and their functions in neurodegenerative diseases and the central nervous system have been identified (Kosik 2006; Maes et al. 2009), Among them, miR-29a and miR-29b are known to be involved in the pathophysiology pathway for the deposition of the amyloid beta (Aβ) plaques and neurofibrillary tangles in the brain of the patients suffering from the Alzheimer's disease (AD) (Delay et al. 2012; Hebert et al. 2008). A decrease in the expression levels of miR-29a and miR-29b facilitates the expression of the Aβ protein precursor (AβPP) and the β-site AβPP-cleaving enzyme (BACE1) in the AD brain, which results in a tremendous increase in the formation of toxic Aβ peptides. The alteration of the miR-29 expression levels is observed not only in the AD brain, but also in biological fluids, such as blood and the cerebrospinal fluid (CSF)(Cogswell et al. 2008). It has been found that miR-29 is tremendously higher in the CSF of AD patients than that of normal individuals(Kiko et al. 2014). Hence, miR-29 can be regarded as an AD-specific biomarker, and its simple, rapid, and sensitive detection from biological fluids is of great significance for the early diagnosis and therapy of AD.

Several standard methods, including the Northern blotting (Lagos-Quintana et al. 2001), microarrays (Thomson et al. 2004), and real-time quantitative polymerase chain reaction (RT-qPCR) (Chen et al. 2005). have been widely used to detect miRNAs. However, certain limitations, such as the time-consuming nature of the processes, requirement of large amounts of samples, additional labeling, sophisticated procedures, low specificity, and high cost, have

been recognized in the conventional analytical methods. In addition to these standard methods, new approaches, including fluorescence (Neely et al. 2006) and bioluminescence assays (Cissell et al. 2008), enzymatic assays (Allawi et al. 2004; Hartig et al. 2004; Su et al. 2007; Wu et al. 2020; Xiong et al. 2020), bead-based profiling (Lu et al. 2005), gold nanoparticle-based colorimetric assay (Yang et al. 2008), nanoquenchers-based fluorescent detection (Koike et al. 2017; Li et al. 2011; Tian et al. 2015; Wang et al. 2011), and exponential isothermal amplification (Jia et al. 2010; Liu et al. 2012; Van Ness et al. 2003; Zhang and Zhang 2012), hybridization chain reaction amplification (Ge et al. 2020), or rolling-circle amplification assays (Liu et al. 2013) have been proposed to circumvent the limitations of the conventional standard methods. In addition, some miRNAs in living cells were detected by MoS_2 quantum dots (Ge et al. 2020), enzyme-MOF composites (Xiong et al. 2020), and DNAzyme nanoprobes (Wu et al. 2020). However, it remains an immense challenge to develop a simple, rapid, cost-effective, and sensitive approach for the specific detection of short miRNAs that are associated with AD from biological fluids, such as the human blood and CSF. In particular, a few analytical methods for the specific and sensitive detection of miR-29 for AD diagnosis have now been reported (Jumeaux et al. 2018; Muller et al. 2016).

Transition metal dichalcogenides (TMDs) are an emerging class of layered nanomaterials of which physicochemical properties are strongly dependent on the composition and dimension (Chhowalla et al. 2013; Manzeli et al. 2017; Wang et al. 2012). The electronic structures and surface activities of the TMDs can be fine-tuned by reducing the number of layers to monolayers (Mak et al. 2010; Zhao et al. 2013), which enables them to be the attractive nanomaterials for application in various research fields (Huang et al. 2013; Lopez-Sanchez et al. 2013; Raza et al. 2017; Xu et al. 2017). For biological and medical applications, thin TMD nanosheets have been exploited as sensing and therapeutic nanomaterials due to

their large surface areas, strong Raman scattering signals, and high surface reactivity (Hu et al. 2019a; Hu et al. 2019b; Kalantar-zadeh et al. 2015; Kang et al. 2018; Lin et al. 2014; Ping et al. 2017). WS_2 has widely been employed as a sensing material in fluorescent (Ge et al. 2017; Zuo et al. 2016), electrochemical (Huang et al. 2014; Nasir et al. 2017; Rahmanian et al. 2018), photoelectrochemical (Sui et al. 2019), and surface plasmon resonance (Ouyang et al. 2016) sensing systems for the detection of biomolecules, metal ions, and toxins (Khan et al. 2019). In particular, TMD nanosheets, including WS_2, have exhibited great promise as a fluorescence quencher for the rapid, simple, and selective detection of DNAs and miRNAs in the Förster resonance energy transfer (FRET)-based assays (Balcioglu et al. 2014; Ge et al. 2014a; Ge et al. 2014b; Huang et al. 2015; Kong et al. 2015; Lan et al. 2018; Li et al. 2015; Loo et al. 2016; Lu et al. 2017; Tian et al. 2017; Xi et al. 2014; Xiao et al. 2018; Yuan et al. 2014; Zhang et al. 2015; Zhu et al. 2013). TMD nanosheets can adsorb a dye-labeled single-stranded DNA (ssDNA) by the weak van der Waals forces (Vovusha and Sanyal 2015), leading to fluorescence quenching, whereas a double-stranded DNA (dsDNA) is likely to desorb from the surface of the TMD nanosheets, resulting in the restoration of the quenched fluorescence. These weak van der Waals forces of interactions between the TMD nanosheets and the DNAs are susceptible for perturbations in the TMD surface states. The adsorption and desorption kinetics and thermodynamics of the ssDNA and the dsDNA can be affected by the interfaces of the exfoliated TMD nanosheets, which can eventually determine the sensing performance of the TMD-based FRET sensors to selectively detect targets. Thus, it is of great interest to gain fundamental insight into the effects of the interface states of TMD nanosheets, such as surface charges, hydrophilicity, hydrophobicity, and surface coverage, on the adsorption and desorption processes of DNAs and miRNAs for the TMD-based FRET sensing of target molecules. Moreover, it is of tremendous importance to develop a TMD-based FRET sensor to selectively detect miR-29 from biological fluids for diagnosis of AD,

since no study has reported that the TMD-based FRET sensors can detect an AD-specific miRNA.

In this study, we modulated the interface of WS_2 nanosheets by their direct exfoliation and functionalization with various types of modified dextran polymers that bear a hydrophilic group, an aromatic ring, a negative charge, or a positive charge in an aqueous solution. The simultaneous exfoliation and functionalization approach produced the four different polymeric interfaces on the WS_2 nanosheets, such as the pristine dextran-functionalized WS_2 (dex-WS_2), the phenoxy dextran-functionalized WS_2 (PhO-dex-WS_2), the carboxymethyl dextran-functionalized WS_2 (CM-dex-WS_2), and the trimethylammonium dextran-functionalized WS_2 (TMA-dex-WS_2). The adsorption kinetics of a fluorescein-labeled probe ssDNA (FAM-DNA) and the desorption energies of the FAM-DNA duplex with a target miR-29a were then investigated over the different interfaces of the WS_2 nanosheets. Based on insight into the effects of the interface engineering on the DNA adsorption and desorption processes, the WS_2 nanosheet-based FRET sensor was designed to selectively detect miR-29a against a non-complementary RNA (miR-9) and a single base-mismatched RNA (sm-RNA) in the human serum.

2. Experimental Methods

2.1 Preparation of the WS_2 nanosheets with different polymeric interfaces.

30.0 mg of dextran, PhO-dex, CM-dex, or TMA-dex was dissolved in 30 mL of water, in which 150.0 mg of the bulk WS_2 was added. The resulting mixture was sonicated using a probe tip sonicator (12 watts) with a pulse sequence of 2 sec-off and 4 sec-on for 1 h in an ice bath. The sonicated solution was then centrifuged using a cascade centrifugation method. The

sonicated solution was first centrifuged at 2,000 x *g* for 1 h to obtain the supernatant. The obtained supernatant was then centrifuged once again at 2,000 x *g* for 1 h to remove the unexfoliated WS_2. Next, the supernatant was centrifuged at 3,500 x *g* for 2 h to obtain the sediment.

2.2 Measurement of the adsorption energies of FMA-DNA on WS_2 nanosheets.

200 μL of the WS_2 nanosheets (300 nM of Dex-WS_2 and 80 nM of PhO-dex-WS_2, CM-dex-WS_2, or TMA-dex-WS_2) was placed in an ITC cell. 2.5 μL of the FAM-DNA (600 nM) was titrated into the WS_2 solution 25-30 times until the temperature of the reaction mixture reached 25°C. The molar concentration of the WS_2 nanosheets was calculated based on an average size obtained by TEM (Mounet et al. 2018). From the fitting curves in ITC, K_a, ΔH, ΔS, and ΔG were automatically obtained. The dissociation constant K_D was calculated by the equation, $K_D = 1/K_a$.

2.3 Detection of miR-29a on the WS_2 nanosheets with different polymeric interfaces.

40 μL of the FMA-DNA (40 nM) and 40 μL of the WS_2 nanosheets (80 μg/mL) were added to 80 μL of Tri-HCl buffer (10 mM, pH 7.4), in which the final concentration of the WS_2 nanosheets was 20 μg/mL. After incubation of the mixture solution for 40 min at 25°C, 28 μL portion of the miR-29a solution was added at desired concentrations. Then, the resulting mixture was incubated at 25°C for 60 min, and the PL spectrum of the FAM-DNA was measured. To detect miR-29a in the human serum, each concentration of miR-29a was increased in the human serum with 2.5 v/v% of Tri-HCl buffer. For the selectivity test, the NC-RNA and the SM-RNA were added into a mixture of the WS_2 nanosheets and the FAM-DNA, instead of miR-29a.

3. Results and Discussion

3.1 Exfoliation and Functionalization of the WS_2 Nanosheets with Functional Polymers.

To prepare the different interfaces of the WS_2 nanosheets, dextran was modified with the phenoxy (PhO-dex), the carboxylmethyl (CM-dex), or the tetramethylammonium (TMA-dex) groups by a simple nucleophilic substitution and ring-opening reactions, as shown in Figure S1. Since biomolecular interactions can be affected by hydrogen bonding, hydrophobic and electrostatic forces, these four different polymers with hydroxyl groups, hydrophobic rings, negative charge, or positive charge were chosen to modulate the interface of the WS_2 nanosheets. The chemical structures of the modified dextran polymers were confirmed by the Fourier-transform infrared (FT-IR) spectroscopy. The PhO-dex polymer showed asymmetric and symmetric stretching modes for aromatic C=C bonds at 1598 cm^{-1} and 1493 cm^{-1} in its FT-IR spectrum (Figure S2, pink line). The CM-dex polymer displayed asymmetric and symmetric stretching modes for the C=O bond of the carboxylate at 1600 cm^{-1} and 1410 cm^{-1} in its FT-IR spectrum (green line), while TMA-dex exhibited characteristic N-C stretching and bending modes at 1592 cm^{-1}, respectively, in its spectrum (blue line). The contents of the phenoxy, carboxyl, and ammonium groups on the modified dextran polymers were quantified using ultraviolet (UV) spectroscopy, base titration, and N elemental analysis, respectively, as depicted in the experimental methods of the Supporting Information (Table S1).

Then, the four different polymers, which included the pristine dextran, the PhO-dex, the CM-dex, and the TMA-dex, were used for the simultaneous exfoliation and functionalization of the WS_2 nanosheets in an aqueous solution by a liquid-phase exfoliation method (Figure 1a) (Backes et al. 2016; Yim et al. 2018; Zong et al. 2017). The pristine dextran was effective for the exfoliation and functionalization of the WS_2 nanosheets (denoted "dex-WS_2") in water via multivalent hydrogen bonding between the hydroxyl groups of the polymer and the chalcogen of WS_2, as previously reported (Kang et al. 2018). However, no WS_2 nanosheet was obtained

without the addition of the polymer in water (Figure 1b). The PhO-dex with a hydrophobic aromatic ring was found to be most effective for the simultaneous exfoliation and functionalization of the WS_2 nanosheets (denoted "PhO-dex-WS_2") in water (108.5 μg/mL), as its concentration was measured by inductively coupled plasma–atomic emission spectroscopy (ICP-AES) (Figure 1c). The CM-dex polymer with a negative charge could exfoliate the WS_2 nanosheets (denoted "CM-dex-WS_2") at a higher concentration (59.4 μg/mL) than the exfoliation done by the pristine dextran (36.9 μg/mL). The TMA-dex polymer with a positive charge also produced the WS_2 nanosheets (TMA-dex-WS_2) at a moderate concentration in water (45.0 μg/mL). In addition, all of the functionalized WS_2 nanosheets exhibited excellent colloidal stability in aqueous solutions for a while (Figure S3).

The physical structures of the functionalized WS_2 nanosheets (dex-WS_2, PhO-dex-WS_2, CM-dex-WS_2, and TMA-dex-WS_2) were analyzed by transmission electron microscopy (TEM), atomic force microscopy (AFM), and scanning electron microscopy (SEM). As shown in Figure 2a-2d and Figure S4, all the WS_2 nanosheets with different polymeric interfaces had a sheet structure with an average lateral size of 65 nm. The thicknesses of the functionalized WS_2 nanosheets, which were analyzed by their height profiles in the AFM images (Figure 2e-2h), were found to be thicker (ca. 4.5 nm) than that of the reported bare WS_2 monolayer (0.85 nm) (Vega-Mayoral et al. 2016), indicating that the functional dextran polymers were adsorbed on the surface of the WS_2 nanosheets (Figure 2i-2l). The surface morphology of the functionalized WS_2 nanosheets was further characterized by SEM (Figure S5). The surface of the functionalized WS_2 nanosheet became very rough compared to that of bulk WS_2, indicating that indicate the polymer interfaces were successfully introduced on the WS_2 nanosheet.

The chemical structures of the WS_2 nanosheets with different polymeric interfaces were

analyzed by X-ray photoelectron spectroscopy (XPS) and FT-IR spectroscopy. As shown in the W4f XPS spectra (Figure 3a and Figure S6), the strong peaks for W^{4+} were clearly observed at 34.7 and 32.8 eV, indicating that all the functionalized WS_2 nanosheets retained an original semiconducting phase after their exfoliation and functionalization in water. The different polymeric interfaces on the WS_2 nanosheets were clearly observed in their FT-IR spectra (Figure 3b). The characteristic vibrational modes for the O–H, C–H, and C–O–C bonds of dextran appeared at 3352, 1456, and 1046 cm^{-1}, respectively, in the FT-IR spectrum of the dex-WS_2 (gray line), which demonstrated that the WS_2 surface was functionalized by the pristine dextran via multivalent hydrogen bonding, as previously reported (Kang et al. 2018). PhO-dex-WS_2 exhibited clear peaks for the aromatic C=C bonds of the phenoxy group at 1559 and 1492 cm^{-1} along with the dextran peaks in its FT-IR spectrum (pink line), while the CM-dex-WS_2 displayed characteristic peaks for carboxylate at 1728 and 1600 cm^{-1} in the spectrum (green line). The TMA-dex-WS_2 also showed characteristic peaks for the CH_3-R bending of the quaternary ammonium at 1372 cm^{-1} (blue line). The four different interfaces of the functionalized WS_2 nanosheets were additionally confirmed by XPS (Figure S7). The characteristic chemical bonds of the modified dextran polymers were evident in the XPS spectra of the dex-WS_2, the PhO-dex-WS_2, the CM-dex-WS_2, and the TMA-dex-WS_2. The C-O and C-C bonds of dextran appeared at 286.3 and 284.7 eV in the C1s XPS spectrum of the dex-WS_2, while the C=C bond of PhO-dex was evident at 288.9 eV in the spectrum of PhO-dex-WS_2. In addition, the C=O bond of the CM-dex and the quaternary C-N bond of the TMA-dex appeared at 288.5 and 285.6 eV, respectively, in the XPS spectra of the CM-dex-WS_2 and the TMA-dex-WS_2. These results show that the four different polymeric interfaces on the WS_2 nanosheets have been successfully prepared via simultaneous exfoliation and functionalization in water.

The surface charges of the functionalized WS_2 nanosheets were then measured at a pH of 7.4 by electrophoretic light scattering. The zeta potential of the bulk WS_2 was found to be −55 eV, which exhibited a large negative charge (Figure 3c). However, the surface negative charges of the dex-WS_2 and the PhO-dex-WS_2 significantly diminished to −5.6 and −12.8 eV, respectively, which can be ascribed to the sufficient coverage of the WS_2 surface with neutral dextran or the PhO-dex. Particularly, the CM-dex-WS_2 with a carboxyl group exhibited a negative charge (−16.4 eV) larger than those exhibited by the dex-WS_2 and the PhO-dex-WS_2, whereas the TMA-dex-WS_2 with a trimethylammonium group exhibited a positive charge (+6.2 eV). These results reveal that the functionalized WS_2 nanosheets have different polymeric interfaces, which influence the adsorption kinetics and thermodynamics of DNAs and miRNAs on the nanosheet surfaces.

3.2 Optical properties of WS_2 nanosheets with different interfaces.

The absorption of the WS_2 nanosheets with four different polymeric interfaces was measured. As shown in Figure S8a, all of the functionalized WS_2 nanosheets, including the dex-WS_2, the PhO-dex-WS_2, the CM-dex-WS_2, and the TMA-dex-WS_2, exhibited a more intense A-excitonic peak at 620 nm than exhibited by the bulk WS_2, indicating that they had thin layered structures with a semiconducting 2H phase. In addition, all the functionalized WS_2 nanosheets strongly absorbed visible radiation in a wide range from 400 to 700 nm. Further, they exhibited approximately the same absorption features. The strong absorption features in a visible range can allow effective fluorescence quenching from the FAM-DNA as the functionalized WS_2 nanosheets that were used as a quencher in the FRET-based assays.

The photoluminescence (PL) emission of the WS_2 nanosheets is dependent strongly on their layer number. As shown in Figure S8b and S9, all the functionalized WS_2 nanosheets exhibited clear PL emission at approximately 618 nm, whereas the bulk WS_2 exhibited no

emission, which suggests the production of a direct band gap of the WS_2 monolayers by a simultaneous exfoliation and functionalization approach in water. The different polymeric interfaces induced a slight difference in the emission wavelength maxima of the functionalized WS_2 nanosheets.

The Raman scattering modes of the WS_2 nanosheets are considered excellent indicators to determine the number of layers (Zeng et al. 2013). As shown in Figure S8c, two distinct peaks for the combined in-plane vibrational mode (E^1_{2g}) and longitudinal acoustic mode (2LA(M)) and the out-of-plane vibrational mode (A_{1g}) appeared at 350 and 418 cm^{-1}, respectively. Moreover, the intensity ratios of 2LA(M) to A_{1g} for the four different interfaces (7.04~8.04) were similar to the reported value of the WS_2 monolayer (Zeng et al. 2013), which was much greater than that (0.85) of the bulk WS_2 (Figure S8d). This finding reveals that the WS_2 nanosheets with different polymeric interfaces have similar thicknesses and analogous lateral sizes. Thus, the physical structures of the exfoliated WS_2 nanosheets, such as their thickness and lateral size, may be excluded from the factors that determine the adsorption and desorption processes of DNAs and miRNAs.

3.3 Adsorption kinetics and thermodynamics of a DNA probe.

Next, the adsorption aspect of the fluorescein-labeled DNA probe (FAM-DNA), which is specific for miR-29a, was investigated across the four different interfaces of the WS_2 nanosheets. First, the adsorption kinetics of FAM-DNA on the WS_2 nanosheets was measured by monitoring the fluorescence quenching of the adsorbed FAM-DNA by FRET (Figure 4a). As shown in Figure 4b, the fluorescence of the FAM-DNA (10 mM) was gradually quenched by the CM-dex-WS_2 (20 μg/mL) over time, which indicates that the DNA probe adsorbed on the surface of the WS_2 nanosheets. The other functionalized WS_2 nanosheets, including the TMA-dex-WS_2, the PhO-dex-WS_2, and the dex-WS_2, also caused the fluorescence quenching

of the FAM-DNA (Figure 4c). However, their quenching efficiencies tremendously differed: the CM-dex-WS_2 exhibited the most effective quenching effect (85%), whereas the dex-WS2 and the PhO-dex-WS2 exhibited tremendously lower quenching effects (28 and 36%, respectively). These results indicate that the polymeric interfaces of the WS_2 nanosheets can influence the adsorption kinetics of FAM-DNA on the surface.

The adsorption kinetics of the FAM-DNA over the CM-dex-WS_2, the TMA-dex-WS_2, the PhO-dex-WS_2, and the dex-WS_2 was obtained by calculating their quenching rate constants (k_q) using the Stern-Volmer equation. As shown in Figure 4d, the fluorescence quenching of the FMA-DNA progressively increased with the increased WS_2 concentration. These quenching responses— as a function of the WS_2 concentrations— were re-plotted by the Stern-Volmer equation to obtain the slopes of the plots (Figure S10). After measuring the lifetime (τ_0) of the excited state of the FAM-DNA without a quencher (Figure S11), the quenching rate constants for the four different polymeric interfaces of the WS_2 nanosheets were obtained (Figure 4e). The CM-dex-WS_2 was found to exhibit the largest quenching rate constant (8.13×10^{-3} $nsec^{-1}$ mg^{-1} mL), indicating that the adsorption of FAM-DNA onto the most negatively-charged surface is kinetically favored. The second largest quenching rate constant of the TMA-dex-WS_2 indicates that the adsorption of the FAM-DNA onto the positively-charged surface is more favored than those of the PhO-dex-WS_2 (2.6×10^{-3} $nsec^{-1}$ mg^{-1} mL) and the dex-WS_2 (2.4×10^{-3} $nsec^{-1}$ mg^{-1} mL). Based on the quenching responses, the number of the FAM-DNA quenched by each WS_2 interface was also calculated (Table S2), showing the good correlation with the quenching kinetics.

To understand the adsorption tendency of FAM-DNA over the four different interfaces of the WS_2 nanosheets, its binding affinities to them were calculated by measuring the

thermodynamic properties using isothermal titration calorimetry (ITC). When a large excess of the FAM-DNA (600 nM) was titrated into the solution of CM-dex-WS_2, a large amount of heat was generated, which demonstrated the interaction between the DNA probe and the CM-dex-WS_2 (Figure 5a, blue line). The thermogram of the TMA-dex-WS_2 evidently shows the production of additional heat for the interaction with FAM-DNA, as compared to the titration of the FAM-DNA into the buffer solution that does not contain the nanosheets (Figure 5b, blue line). The binding affinity of the FAM-DNA to the target miRNA miR-29a was also calculated by measuring the heat energy for hybridization (Figure 5c, blue line). The heat energies for the interactions of the FAM-DNA with the PhO-dex-WS_2 and dex-WS_2 were measured as well (Figure S12). After fitting the heat energies with molar ratios (Figure 5d-5f), the binding affinities of the FAM-DNA against the four different WS_2 nanosheets and miR-29a were obtained with several thermodynamic parameters (Figue 5g). The dissociation constant of the CM-dex-WS_2 for the FAM-DNA was 0.38 nM, which was tremendously smaller than that of the target miR-29a (1.25 nM). In addition, the CM-dex-WS_2 had a lower dissociation constant than that of the TMA-dex-WS_2 (6.13 nM) for the FAM-DNA. These results reveal that the CM-dex-WS_2 exhibits the highest binding affinity to the FAM-DNA, followed by the binding affinities exhibited by the TMA-dex-WS_2, the PhO-dex-WS_2, and the dex-WS_2. These binding affinities are in accordance with the adsorption rate constants of the FAM-DNA across the four different interfaces of the WS_2 nanosheets.

It has been reported that the predominant interaction of DNA with WS_2 or MoS_2 nanosheets is due to the van der Waals force (Sharma et al. 2016; Vovusha and Sanyal 2015), which is normally very weak. The binding affinities of the CM-dex-WS_2 and the TMA-dex-WS_2 to the FAM-DNA, however, were measured to be much higher than that of the van der Waals interactions, as shown in Figure 5g. Thus, these higher binding affinities indicate that the FAM-DNA can adsorb on the polymeric interface rather than on the WS_2 surface. To

indirectly verify this hypothesis, the binding affinities of the free polymers, such as CM-dex and TMA-dex, against the FAM-DNA were measured by ITC. As shown in Figure S13, the binding affinities of the CM-dex and the TMA-dex for the FAM-DNA were found to be very high. In addition, the binding affinity of the free CM-dex against the FAM-DNA was higher than that of the free TMA-dex, of which tendency corresponds to that observed in CM-dex-WS_2 and TMA-dex-WS_2 nanosheets. This clearly implicates that the FAM-DNA probe adsorbs on the polymeric phases of the WS_2 nanosheets, rather than on the WS_2 surface.

To further understand the binding forces between WS_2 nanosheet interfaces and FAM-DNA, several small molecules such as phosphate to disrupt charge interaction, urea to disturb hydrogen bonding, and four nucleobases were added into the TMA-dex-WS_2 or CM-dex-WS_2 adsorbing FAM-DNA as reported in the previous study (Meng et al. 2018). As shown in Figure S14, the addition of either phosphate or urea into the TMA-dex-WS_2 or CM-dex-WS_2 adsorbing FAM-DNA induced the turn-on fluorescence response, indicating that charge interaction and hydrogen bonding would be involved in the adsorption process of FAM-DNA on the WS_2 interface. Furthermore, the addition of a nucleobase monomer caused the turn-on fluorescence response in the CM-dex-WS_2 bearing FAM-DNA. These experimental results suggest that the multiple interactions, including charge interaction and hydrogen bonding, rather than single one would be involved in the adsorption of FAM-DNA on WS_2 nanosheets interfaces.

3.4 Detection of an AD biomarker miR-29a.

Based on the kinetic and thermodynamic parameters of the four different WS_2 nanosheets for the FAM-DNA adsorption, the CM-dex-WS_2 and the TMA-dex-WS_2 were chosen as quenchers to further investigate miR-29a detection. As shown in Figure 6a, the DNA probe (FAM-DNA) was first adsorbed on the CM-dex-WS_2 or the TMA-dex-WS_2, and then the

complementary target miR-29a (80 nM) was added into the mixture solution to induce its hybridization with FMA-DNA. As shown in Figure 6b (black line), the fluorescence of the FAM-DNA was significantly quenched in the presence of TMA-dex-WS_2. However, addition of miR-29a into the quenched solution induced a large recovery in the quenched fluorescence (green line), which suggests the desorption of the duplex of FAM-DNA and miR-29a from the surface of the TMA-dex-WS_2. Adding the same volume of PBS did not induce recovery in the quenched fluorescence of the FAM-DNA adsorbed on the TMA-dex-WS_2 (Figure 6c and S15a). The CM-dex-WS_2 significantly quenched the fluorescence of FAM-DNA via a strong adsorption; however, the quenched fluorescence was barely recovered in the presence of the target miR-29a (Figure 6c and S15b). This indicates that the FAM-DNA adsorbed on the CM-dex-WS_2 was not effectively desorbed from the surface of the nanosheets after its hybridization with miR-29a. The better turn-on response of the TMA-dex-WS_2 than that of the CM-dex-WS_2 to miR-29a can be understood by their binding affinities to the FAM-DNA, as shown in Figure 5g. The binding affinity of the TMA-dex-WS_2 to the FAM-DNA was lower than that of the FAM-DNA to miR-29a, which leads to the effective desorption of the adsorbed FAM-DNA after its hybridization with miR-29a. However, the binding affinity of the CM-dex-WS_2 to the FAM-DNA was higher than that of the FAM-DNA to miR-29a. Thus, the adsorption of FAM-DNA onto the CM-dex-WS_2 is thermodynamically more favored than its hybridization with miR-29a, which leads to a weak turn-on response of the quenched fluorescence due to the low desorption efficiency of the FAM-DNA from the nanosheet surface.

TMA-dex-WS_2 was selected as the most effective interface for FRET-based sensing of miR-29a. As shown in Figure 6d, the quenched fluorescence of the FAM-DNA adsorbed on the TMA-dex-WS_2 was gradually restored as the concentration of miR-29a increased, which showed that this turn-on fluorescence response was induced by the target miRNA. In addition,

a non-complimentary RNA (NC-RNA: 5′-AUAAAGCUAGAUAACCGAAAGU-3′, Table S3) barely induced recovery in the quenched fluorescence of the FAM-DNA on the TMA-dex-WS_2 (Figure 6e). Particularly, a single base-mismatched RNA (SM-RNA: 5′-UAGCACCAUCUAAAAUCGGUUA-3′) induced a tremendously smaller recovery in the quenched fluorescence of the FAM-DNA on the TMA-dex-WS_2 than that of the complementary target miR-29a. These results indicate that the TMA-dex-WS_2-based FRET sensor can selectively detect the target miRNA (miR-29a) that is specific for AD by its turn-on fluorescence.

Lastly, the TMA-dex-WS_2 FRET sensor was used to detect miR-29a in the human serum. As shown in Figure S16, the A-excitonic absorbance of the TMA-dex-WS_2 sensor at 632 nm remained almost constant without aggregation in the human serum solution over time. This result shows that the sensor exhibits a great colloidal stability during a period of assay in human serum. Furthermore, to improve the detection sensitivity of the TMA-dex-WS_2 FRET sensor in human serum, the ratio of FMA-DNA to TMA-dex-WS_2 was varied (Figure S17). The TMA-dex-WS_2 FRET sensor adsorbing a 40 nM of FAM-DNA showed the highest turn-on fluorescence response to miR-29a in human serum. After adsorption of the FAM-DNA onto the TMA-dex-WS_2 under the optical conditions, each spiked serum of miR-29a was added into the sensor solution. As shown in Figure 6f, the quenched fluorescence of the FAM-DNA was progressively restored as the concentration of miR-29a was elevated in the human serum. This finding shows that the TMA-dex-WS_2 FRET sensor can detect the target miRNA that is specific for AD in the human serum by its turn-on fluorescence response. The TMA-dex-WS_2 FRET sensor can detect miR-29a at a concentration as low as 745 pM in human serum. Then, the TMA-dex-WS_2 FRET sensor was employed to quantify the concentration of miR-29a from several spiked human serum samples (Table S4). The sensor could quantify the concentration of miR-29a in each spiked serum sample with a range of

proportional errors using the linear regression equation shown in Figure 6f. The deviation between the spiked and measured concentrations was small to be included in the error ranges of the regression plot. The proportional errors of the TMA-dex-WS_2 FRET sensor, however, could be improved further by modulating its interfaces. The accurate concentration of miR-29a in biological fluids could not be found in clinical data. Other miRNAs were found to occur at nanomolar to picomolar concentrations in clinical samples (Weber et al. 2010). Hence, the detection sensitivity of the TMA-dex-WS_2 FRET sensor might be acceptable for the detection of miR-29a from clinical samples.

The performance of the TMA-dex-WS_2 FRET sensor for the detection of miR-29a was compared with that of previously reported sensing systems. As stated, a few papers for the detection of miR-29a have been reported to date (Table S5). The TMA-dex-WS_2 FRET sensor can detect the target miR-29a more rapidly and simply with excellent sensitivity than the previous sensing systems because no additional amplification process is required in this FRET sensor. Additionally, the performance of the TMA-dex-WS_2 FRET sensor was compared with that of previously reported FRET-based sensors for the detection of various DNAs as well as RNAs (Table S6). It was found that the TMA-dex-WS_2 FRET sensor had comparable assay time, detection sensitivity and selectivity, and a dynamic range of detection with the previous FRET sensors.

4. Conclusions

WS_2 nanosheets were non-covalently functionalized with the dextran polymers using a liquid-phase exfoliation approach, producing the four different WS_2 interfaces. The interface modulation of WS_2 nanosheets induced noticeable changes in the adsorption kinetics and thermodynamics of a FAM-DNA probe. Among them, the CM-dex-WS_2 exhibited a fastest

adsorption rate of the FAM-DNA, causing the effective fluorescence quenching, however, the adsorption strength of the FAM-DNA for the CM-dex-WS_2 was larger than its binding affinity to miR-29a. In contrast, the TMA-dex-WS_2 exhibited fast adsorption kinetics of the FAM-DNA and a proper adsorption strength, which led to its favored desorption from the nanosheet surface after hybridization with the target miR-29a. The TMA-dex-WS_2 FRET sensor selectively detected the AD biomarker miR-29a at a concentration as low as 745 pM against the non-complementary and the single base-mismatched RNA in the human serum. This interface engineering approach can extend to various nanomaterials for the effective sensing and delivery of DNAs and RNAs. In addition, the WS_2 nanosheet-based FRET sensor presents potential as a diagnostic tool to diagnose AD in the non-invasive manner via miRNA detection in blood.

Associated content

The Supporting Information including more supplementary data can be found online at *Biosensors and Bioelectronics*.

Author information

Corresponding Author;

Jong-Ho Kim, e-mail: kjh75@hanyang.ac.kr

Acknowledgements

This work was supported by the Basic Science Research Program (NRF-

2017R1A2B2008455) of the National Research Foundation of Korea, as funded by the Ministry of Science and ICT.

Declaration of competing interest

The authors declare no competing financial interest.

References

Allawi, H.T., Dahlberg, J.E., Olson, S., Lund, E., Olson, M., Ma, W.P., Takova, T., Neri, B.P., Lyamichev, V.I., 2004. Rna 10(7), 1153-1161.

Backes, C., Szydlowska, B.M., Harvey, A., Yuan, S.J., Vega-Mayoral, V., Davies, B.R., Zhao, P.L., Hanlon, D., Santos, E.J.G., Katsnelson, M.I., Blau, W.J., Gadermaier, C., Coleman, J.N., 2016. Acs Nano 10(1), 1589-1601.

Balcioglu, M., Rana, M., Robertson, N., Yigit, M.V., 2014. Acs Appl Mater Inter 6(15), 12100-12110.

Bartel, D.P., 2004. Cell 116(2), 281-297.

Chen, C.F., Ridzon, D.A., Broomer, A.J., Zhou, Z.H., Lee, D.H., Nguyen, J.T., Barbisin, M., Xu, N.L., Mahuvakar, V.R., Andersen, M.R., Lao, K.Q., Livak, K.J., Guegler, K.J., 2005. Nucleic Acids Res 33(20), e179.

Chhowalla, M., Shin, H.S., Eda, G., Li, L.J., Loh, K.P., Zhang, H., 2013. Nature Chemistry 5(4), 263-275.

Cissell, K.A., Rahimi, Y., Shrestha, S., Hunt, E.A., Deo, S.K., 2008. Anal Chem 80(7), 2319-2325.

Cogswell, J.P., Ward, J., Taylor, I.A., Waters, M., Shi, Y.L., Cannon, B., Kelnar, K., Kemppainen, J., Brown, D., Chen, C., Prinjha, R.K., Richardson, J.C., Saunders, A.M., Roses, A.D., Richards, C.A., 2008. J Alzheimers Dis 14(1), 27-41.

Delay, C., Mandemakers, W., Hebert, S.S., 2012. Neurobiol Dis 46(2), 285-290.

Ge, J., Ou, E.C., Yu, R.Q., Chu, X., 2014a. J Mater Chem B 2(6), 625-628.

Ge, J., Qi, Z.Y., Zhang, L.L., Shen, X.P., Shen, Y.M., Wang, W.X., Li, Z.H., 2020. Nanoscale 12(2), 808-814.

Ge, J., Tang, L.J., Xi, Q., Li, X.P., Yu, R.Q., Jiang, J.H., Chu, X., 2014b. Nanoscale 6(12), 6866-6872.

Ge, J., Xin-Geng, Du, Y.H., Chen, J.J., Zhang, L., Bai, D.M., Ji, D.Y., Hu, Y.L., Li, Z.H., 2017. Sensor Actuat B-Chem 249, 189-194.

Hartig, J.S., Grune, I., Najafi-Shoushtari, S.H., Famulok, M., 2004. J Am Chem Soc 126(3), 722-723.

Hebert, S.S., Horre, K., Nicolai, L., Papadopoulou, A.S., Mandemakers, W., Silahtaroglu, A.N., Kauppinen, S., Delacourte, A., De Strooper, B., 2008. P Natl Acad Sci USA 105(17), 6415-6420.

Hu, H.W., Zavabeti, A., Quan, H.Y., Zhu, W.Q., Wei, H.Y., Chen, D.C., Ou, J.Z., 2019a. Biosens Bioelectron 142, 111573.

Hu, X.L., Chu, L.Y., Dong, X.J., Chen, C.R., Tang, T.T., Chen, D.J., He, X.P., Tian, H., 2019b. Adv Funct Mater 29(14), 1806986.

Huang, J.H., Ye, L., Gao, X., Li, H., Xu, J.B., Li, Z.G., 2015. J Mater Chem B 3(11), 2395-2401.

Huang, K.J., Liu, Y.J., Wang, H.B., Gan, T., Liu, Y.M., Wang, L.L., 2014. Sensor Actuat B-Chem 191, 828-836.

Huang, X., Zeng, Z.Y., Zhang, H., 2013. Chem Soc Rev 42(5), 1934-1946.

Ikeda, S., Kong, S.W., Lu, J., Bisping, E., Zhang, H., Allen, P.D., Golub, T.R., Pieske, B., Pu, W.T., 2007. Physiol Genomics 31(3), 367-373.

Jia, H.X., Li, Z.P., Liu, C.H., Cheng, Y.Q., 2010. Angew Chem Int Edit 49(32), 5498-5501.

Jumeaux, C., Wahlsten, O., Block, S., Kim, E., Chandrawati, R., Howes, P.D., Hook, F., Stevens, M.M., 2018. Chembiochem 19(5), 434-438.

Kalantar-zadeh, K., Ou, J.Z., Daeneke, T., Strano, M.S., Pumera, M., Gras, S.L., 2015. Adv Funct Mater 25(32), 5086-5099.

Kang, T.W., Han, J., Lee, S., Hwang, I.J., Jeon, S.J., Ju, J.M., Kim, M.J., Yang, J.K., Jun, B., Lee, C.H., Lee, S.U., Kim, J.H., 2018. Nat Commun 9, 2549.

Khan, I.M., Niazi, S., Yu, Y., Mohsin, A., Mushtaq, B.S., Iqbal, M.W., Rehman, A., Alhtar, W., Wang, Z.P., 2019. Anal Chem 91(21), 14085-14092.

Kiko, T., Nakagawa, K., Tsuduki, T., Furukawa, K., Arai, H., Miyazawa, T., 2014. J Alzheimers Dis 39(2), 253-259.

Koike, M., Asakura, Y., Sugihara, M., Kuroda, Y., Tsuzura, H., Wada, H., Shimojima, A., Kuroda, K., 2017. Dalton T 46(31), 10232-10239.

Kong, R.M., Ding, L., Wang, Z.J., You, J.M., Qu, F.L., 2015. Analytical and Bioanalytical Chemistry 407(2), 369-377.

Kosik, K.S., 2006. The neuronal microRNA system. Nat Rev Neurosci 7(12), 911-920.

Lagos-Quintana, M., Rauhut, R., Lendeckel, W., Tuschl, T., 2001. Science 294(5543), 853-858.

Lan, L.Y., Chen, D.K., Yao, Y., Peng, X.S., Wu, J., Li, Y.B., Ping, J.F., Ying, Y.B., 2018. Acs Appl Mater Inter 10(49), 42009-42017.

Li, B.L., Zou, H.L., Lu, L., Yang, Y., Lei, J.L., Luo, H.Q., Li, N.B., 2015. Adv Funct Mater 25(23), 3541-3550.

Li, H.L., Zhang, Y.W., Luo, Y.L., Sun, X.P., 2011. Small 7(11), 1562-1568.

Lin, T.R., Zhong, L.S., Guo, L.Q., Fu, F.F., Chen, G.N., 2014. Nanoscale 6(20), 11856-11862.

Liu, H.Y., Li, L., Duan, L.L., Wang, X., Xie, Y.X., Tong, L.L., Wang, Q., Tang, B., 2013. Anal Chem 85(16), 7941-7947.

Liu, Y.Q., Zhang, M., Yin, B.C., Ye, B.C., 2012. Anal Chem 84(12), 5165-5169.

Loo, A.H., Bonanni, A., Pumera, M., 2016. Analyst 141(15), 4654-4658.

Lopez-Sanchez, O., Lembke, D., Kayci, M., Radenovic, A., Kis, A., 2013. Nat Nanotechnol 8(7), 497-501.

Lu, C., Liu, Y.B., Ying, Y.B., Liu, J.W., 2017. Langmuir 33(2), 630-637.

Lu, J., Getz, G., Miska, E.A., Alvarez-Saavedra, E., Lamb, J., Peck, D., Sweet-Cordero, A., Ebet, B.L., Mak, R.H., Ferrando, A.A., Downing, J.R., Jacks, T., Horvitz, H.R., Golub, T.R., 2005. Nature 435(7043), 834-838.

Maes, O.C., Chertkow, H.M., Wang, E., Schipper, H.M., 2009. Curr Genomics 10(3), 154-168.

Mak, K.F., Lee, C., Hone, J., Shan, J., Heinz, T.F., 2010. Phys Rev Lett 105(13).

Manzeli, S., Ovchinnikov, D., Pasquier, D., Yazyev, O.V., Kis, A., 2017. Nature Reviews Materials 2(8), 17033.

Meng, Y.C., Liu, P., Zhou, W.H., Ding, J.S., Liu, J.W., 2018. Acs Nano 12(9), 9070-9080.

Mitchell, P.S., Parkin, R.K., Kroh, E.M., Fritz, B.R., Wyman, S.K., Pogosova-Agadjanyan, E.L., Peterson, A., Noteboom, J., O'Briant, K.C., Allen, A., Lin, D.W., Urban, N., Drescher, C.W., Knudsen, B.S., Stirewalt, D.L., Gentleman, R., Vessella, R.L., Nelson, P.S., Martin, D.B., Tewari, M., 2008. P Natl Acad Sci USA 105(30), 10513-10518.

Mounet, N., Gibertini, M., Schwaller, P., Campi, D., Merkys, A., Marrazzo, A., Sohier, T., Castelli, I.E., Cepellotti, A., Pizzi, G., Marzari, N., 2018. Nat Nanotechnol 13(3), 246.

Muller, M., Jakel, L., Bruinsma, I.B., Claassen, J.A., Kuiperij, H.B., Verbeek, M.M., 2016. Mol Neurobiol 53(5), 2894-2899.

Nasir, M.Z.M., Mayorga-Martinez, C.C., Sofer, Z., Pumera, M., 2017. Acs Nano 11(6), 5774-5784.

Neely, L.A., Patel, S., Garver, J., Gallo, M., Hackett, M., McLaughlin, S., Nadel, M., Harris, J., Gullans, S., Rooke, J., 2006. Nat Methods 3(1), 41-46.

Ouyang, Q.L., Zeng, S.W., Jiang, L., Hong, L.Y., Xu, G.X., Dinh, X.Q., Qian, J., He, S.L., Qu, J.L., Coquet, P., Yong, K.T., 2016. Sci Rep-Uk 6, 28190.

Ping, J.F., Fan, Z.X., Sindoro, M., Ying, Y.B., Zhang, H., 2017. Adv Funct Mater 27(19), 1605817.

Rahmanian, E., Mayorga-Martinez, C.C., Malekfar, R., Luxa, J., Sofer, Z., Pumera, M., 2018. Acs Appl Nano Mater 1(12), 7006-7015.

Raza, F., Yim, D., Park, J.H., Kim, H.I., Jeon, S.J., Kim, J.H., 2017. J Am Chem Soc 139(41), 14767-14774.

Sempere, L.F., Freemantle, S., Pitha-Rowe, I., Moss, E., Dmitrovsky, E., Ambros, V., 2004. Genome Biol 5(3), R13.

Sharma, M., Kumar, A., Ahluwalia, P.K., 2016. Rsc Adv 6(65), 60223-60230.

Su, X., Teh, H.F., Lieu, X.H., Gao, Z.Q., 2007. Anal Chem 79(18), 7192-7197.

Sui, C.J., Wang, T.T., Zhou, Y.L., Yin, H.S., Meng, X.J., Zhang, S.R., Waterhouse, G.I.N., Xu, Q., Zhuge, Y.P., Ai, S.Y., 2019. Biosens Bioelectron 127, 38-44.

Thomson, J.M., Parker, J., Perou, C.M., Hammond, S.M., 2004. Nat Methods 1(1), 47-53.

Tian, F., Lyu, J., Shi, J.Y., Yang, M., 2017. Biosens Bioelectron 89, 123-135.

Tian, J.Q., Cheng, N.Y., Liu, Q., Xing, W., Sun, X.P., 2015. Angew Chem Int Edit 54(18), 5493-5497.

Van Ness, J., Van Ness, L.K., Galas, D.J., 2003. P Natl Acad Sci USA 100(8), 4504-4509.

Vega-Mayoral, V., Backes, C., Hanlon, D., Khan, U., Gholamvand, Z., O'Brien, M., Duesberg, G.S., Gadermaier, C., Coleman, J.N., 2016. Adv Funct Mater 26(7), 1028-1039.

Vovusha, H., Sanyal, B., 2015. Rsc Adv 5(83), 67427-67434.

Wang, L., Zhang, Y.W., Tian, J.Q., Li, H.L., Sun, X.P., 2011. Nucleic Acids Res 39(6), e37.

Wang, Q.H., Kalantar-Zadeh, K., Kis, A., Coleman, J.N., Strano, M.S., 2012. Nat Nanotechnol 7(11), 699-712.

Weber, J.A., Baxter, D.H., Zhang, S.L., Huang, D.Y., Huang, K.H., Lee, M.J., Galas, D.J., Wang, K., 2010. Clin Chem 56(11), 1733-1741.

Wu, Y.N., Meng, H.M., Chen, J., Jiang, K.M., Yang, R., Li, Y.Y., Zhang, K., Qu, L.B., Zhang, X.B., Li, Z.H., 2020. Chem Commun 56(3), 470-473.

Xi, Q., Zhou, D.M., Kan, Y.Y., Ge, J., Wu, Z.K., Yu, R.Q., Jiang, J.H., 2014. Anal Chem 86(3), 1361-1365.

Xiao, M.S., Chandrasekaran, A.R., Ji, W., Li, F., Man, T.T., Zhu, C.F., Shen, X.Z., Pei, H., Li, Q., Li, L., 2018. Acs Appl Mater Inter 10(42), 35794-35800.

Xiong, M.Y., Zhang, M., Liu, Q., Yang, C., Xie, Q.J., Ke, G.L., Meng, H.M., Zhang, X.B., Tan, W.H., 2020. Chem Commun 56(19), 2901-2904.

Xu, J., Zhang, J.J., Zhang, W.J., Lee, C.S., 2017. Adv Energy Mater 7(23), 1700571.

Yang, W.J., Li, X.B., Li, Y.Y., Zhao, L.F., He, W.L., Gao, Y.Q., Wan, Y.J., Xia, W., Chen, T., Zheng, H., Li, M., Xu, S.Q., 2008. Anal Biochem 376(2), 183-188.

Yim, D., Kim, J.E., Kim, H.I., Yang, J.K., Kang, T.W., Nam, J., Han, S.H., Jun, B., Lee, C.H., Lee, S.U., Kim, J.W., Kim, J.H., 2018. Small 14(16), e1800026.

Yuan, Y.X., Li, R.Q., Liu, Z.H., 2014. Anal Chem 86(7), 3610-3615.

Zeng, H.L., Liu, G.B., Dai, J.F., Yan, Y.J., Zhu, B.R., He, R.C., Xie, L., Xu, S.J., Chen, X.H., Yao, W., Cui, X.D., 2013. Sci Rep-Uk 3, 1608.

Zhang, Y., Zhang, C.Y., 2012. Anal Chem 84(1), 224-231.

Zhang, Y., Zheng, B., Zhu, C.F., Zhang, X., Tan, C.L., Li, H., Chen, B., Yang, J., Chen, J.Z., Huang, Y., Wang, L.H., Zhang, H., 2015. Adv Mater 27(5), 935-939.

Zhao, W.J., Ghorannevis, Z., Chu, L.Q., Toh, M.L., Kloc, C., Tan, P.H., Eda, G., 2013. Acs Nano 7(1), 791-797.

Zhu, C.F., Zeng, Z.Y., Li, H., Li, F., Fan, C.H., Zhang, H., 2013. J Am Chem Soc 135(16), 5998-6001.

Zong, L., Li, M.J., Li, C.X., 2017. Adv Mater 29(10), 1604691.

Zuo, X.W., Zhang, H.G., Zhu, Q., Wang, W.F., Feng, J., Chen, X.G., 2016. Biosens Bioelectron 85, 464-470.

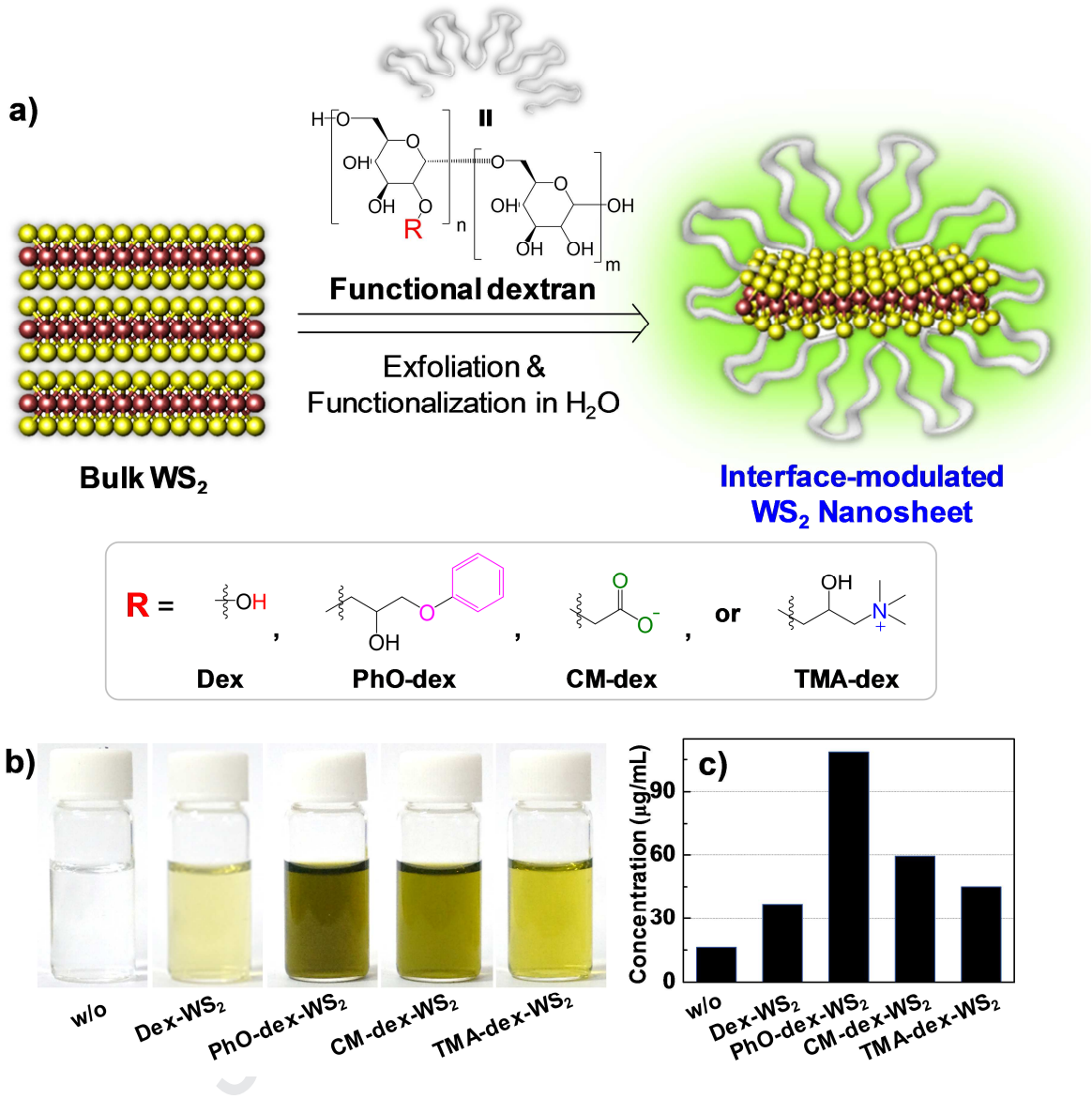

Figure 1. Functionalization of the WS_2 nanosheets with dextran polymers. a) Schematic illustration for the liquid-phase exfoliation of the WS_2 nanosheets with functionalized polymers; dextran (Dex), phenoxy-modified dextran (PhO-dex), carboxymethyl dextran (CM-dex), and tri-methyl ammonium modified dextran (TMA-dex) in H_2O. b) Photographs and c) concentrations of exfoliated WS_2 nanosheets with different polymeric interfaces.

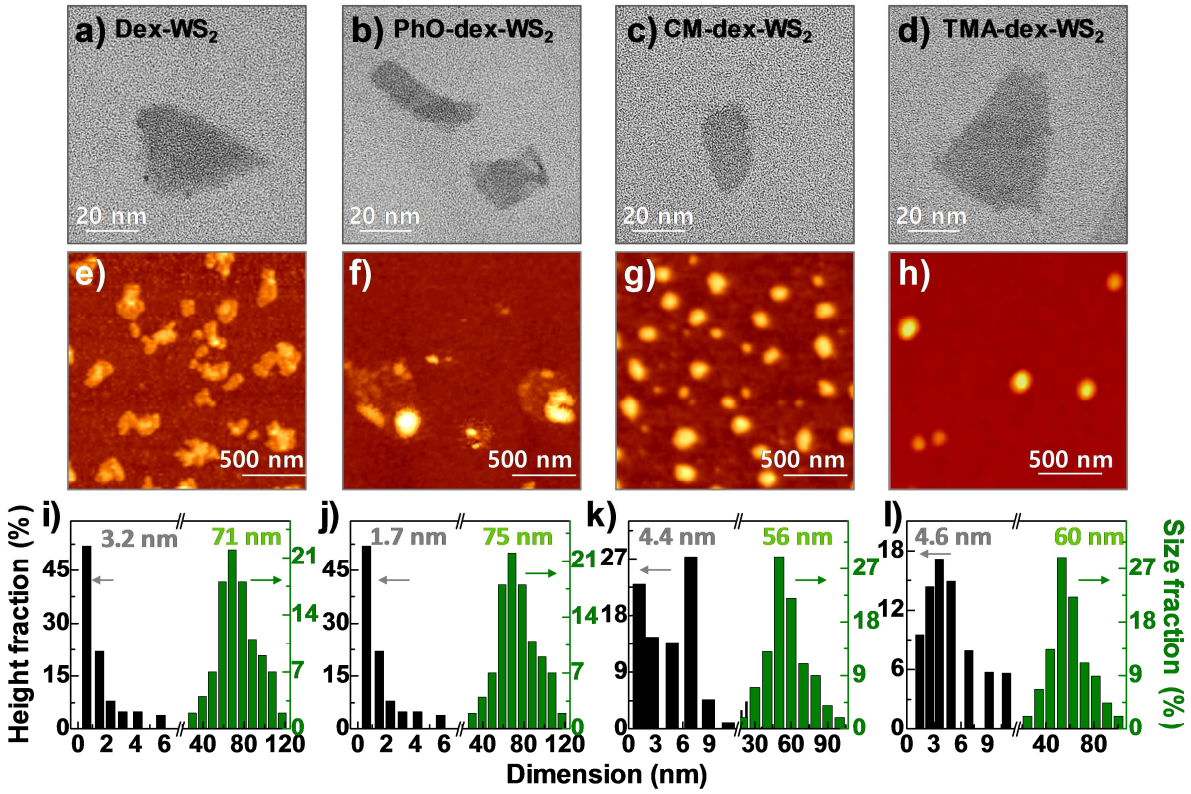

Figure 2. Physical structures of the WS_2 nanosheets with different polymeric interfaces. TEM images of a) the Dex-WS_2, b) the PhO-dex-WS_2, c) the CM-dex-WS_2, and d) the TMA-dex-WS_2. AFM images of e) the Dex-WS_2, f) the PhO-dex-WS_2, g) the CM-dex-WS_2, and h) the TMA-dex-WS_2. Histograms for the thickness and lateral size of i) the Dex-WS_2, j) the PhO-dex-WS_2, k) the CM-dex-WS_2, and l) the TMA-dex-WS_2.

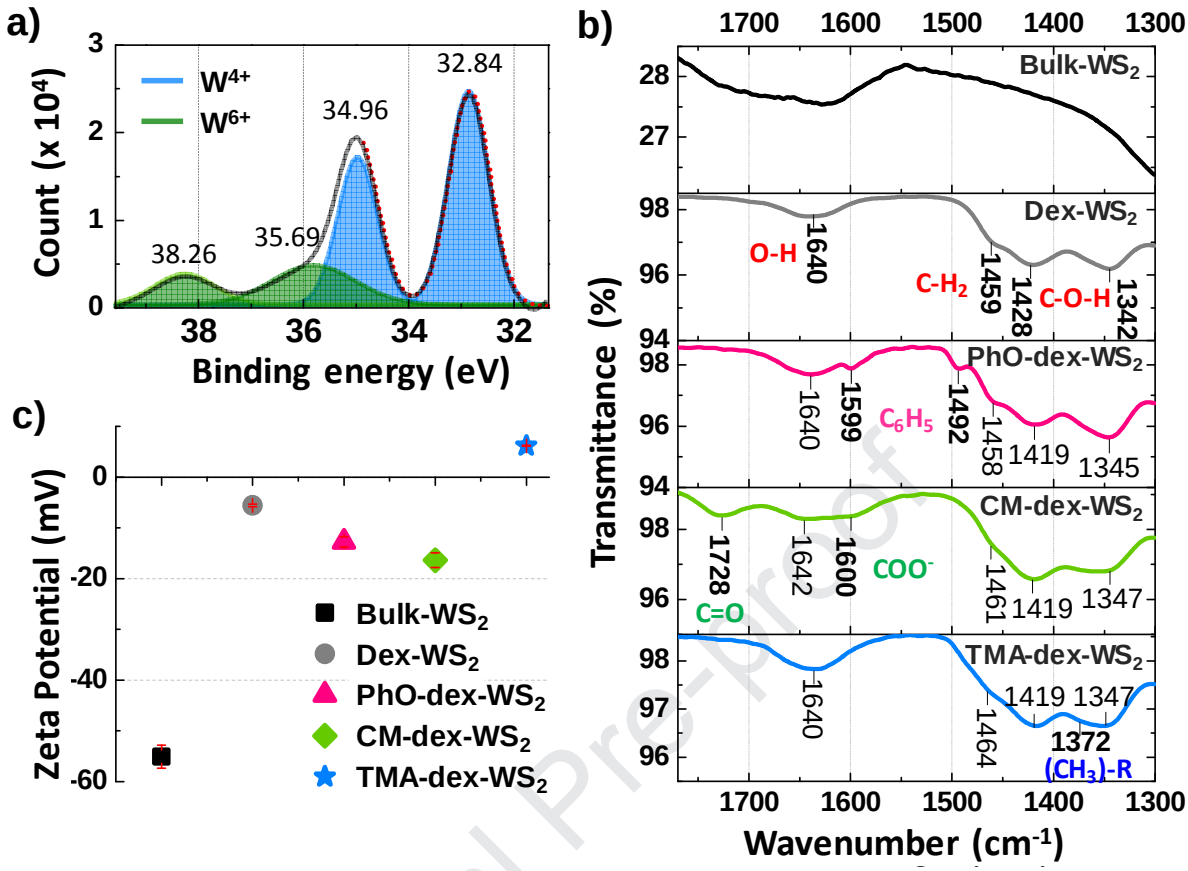

Figure 3. Chemical structures of the WS_2 nanosheets with different polymeric interfaces. a) The W4f XPS spectrum of the CM-dex-WS_2. A gray solid line and a red dashed line represent the original and the fitting spectra, respectively. b) FT-IR spectra and c) the Zeta potentials of the bulk WS_2, the Dex-WS_2, the PhO-dex-WS_2, the CM-dex-WS_2, and the TMA-dex-WS_2.

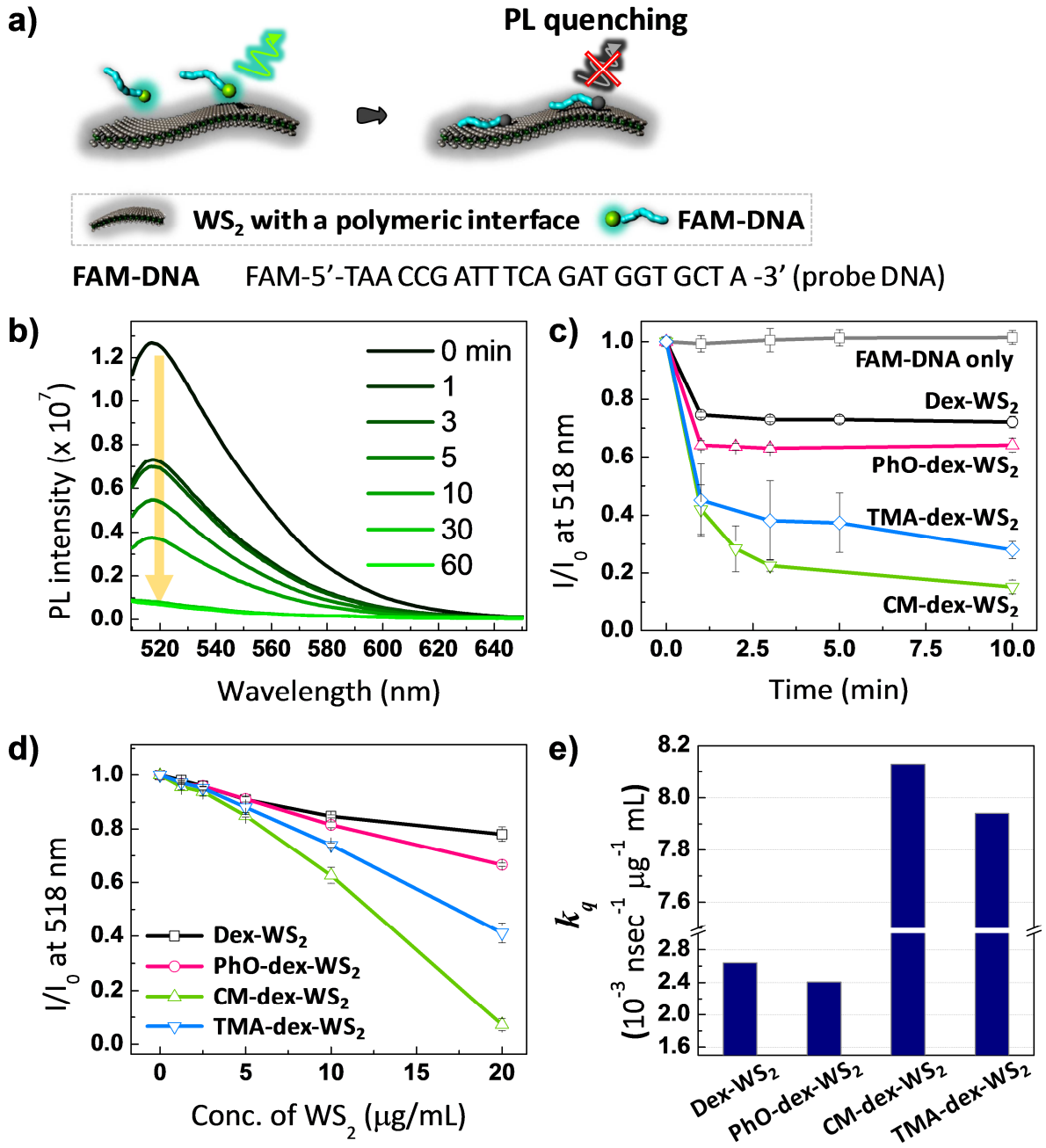

Figure 4. Quenching responses of FAM-DNA to WS_2 nanosheets with different polymeric interfaces. a) Schematic illustration for quenching of the fluorescence of FAM-DNA by a WS_2 nanosheet with a polymeric interface. b) PL responses of FAM-DNA to CM-dex-WS_2 (40 μg/mL) over time. c) PL intensity changes of FAM-DNA at 518 nm in the presence of Dex-WS_2, PhO-dex-WS_2, CM-dex-WS_2, and TMA-dex-WS_2. d) PL intensity changes of FAM-DNA as a function of WS_2 concentrations. e) Quenching rate constants of Dex-WS_2, PhO-dex-WS_2, CM-dex-WS_2, and TMA-dex-WS_2 against FAM-DNA.

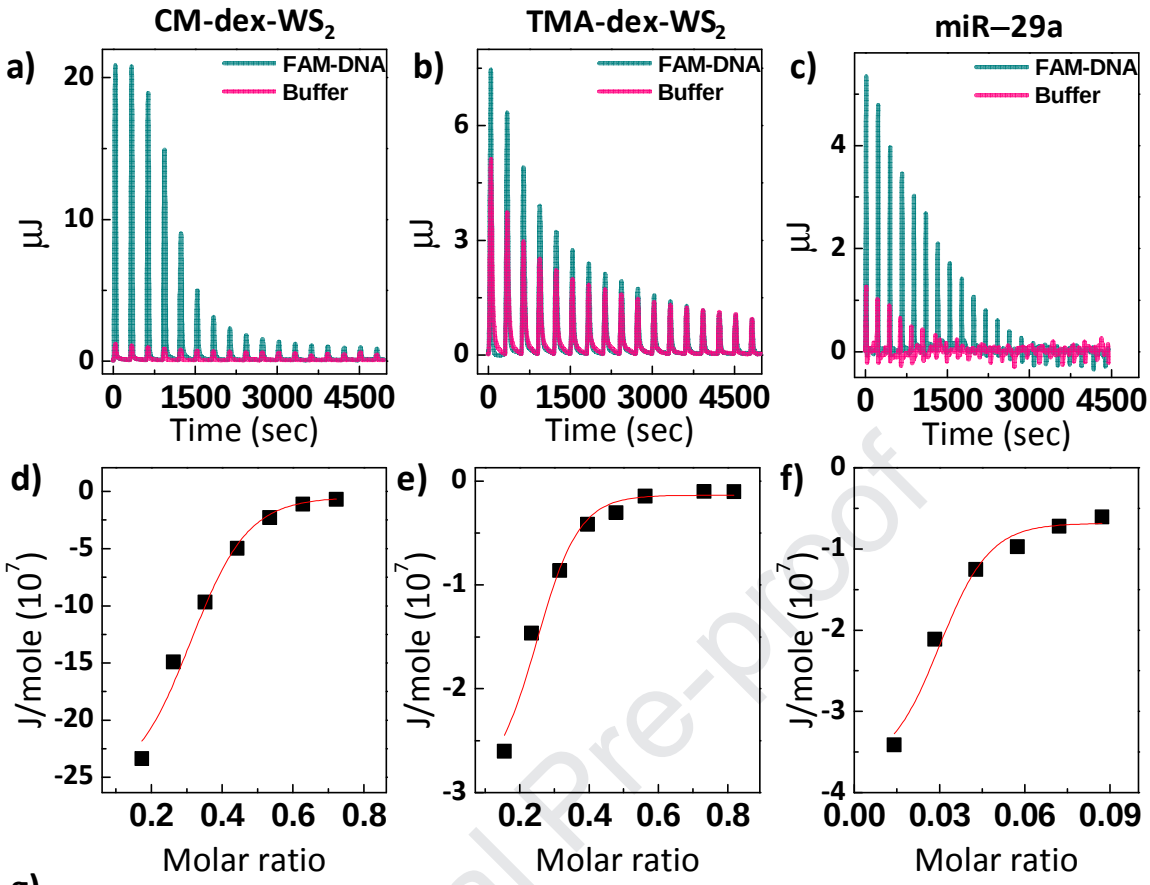

g)

	miR-29a	dex-WS_2	PhO-dex -WS_2	CM-dex -WS_2	TMA-dex -WS_2
K_A (M^{-1})	8.0×10^8	9.9×10^6	4.5×10^7	2.6×10^9	1.6×10^8
ΔH (J/mole)	-4.4×10^7	-4.2×10^6	-9.7×10^6	-1.3×10^8	-2.6×10^7
ΔS (J/mole·K)	-1.5×10^5	-1.4×10^4	-43×10^4	-4.5×10^5	-8.7×10^4
ΔG (J/mole)	-4.1×10^4	-4.0×10^4	-4.4×10^4	-5.4×10^4	-4.7×10^4
K_d (nM)	**1.25**	**100.7**	**22.2**	**0.38**	**6.13**

Figure 5. Measurements of the adsorption energies of FAM-DNA on WS_2 nanosheets with different polymeric interfaces. ITC thermograms of a) CM-dex-WS_2, b) TMA-dex-WS_2, and c) miR-29a. ITC fitting plots for d) CM-dex-WS_2, e) TMA-dex-WS_2, and f) miR-29a. g) Thermodynamic parameters for the adsorption of FAM-DNA on WS_2 nanosheets with different polymeric interfaces measured by ITC.

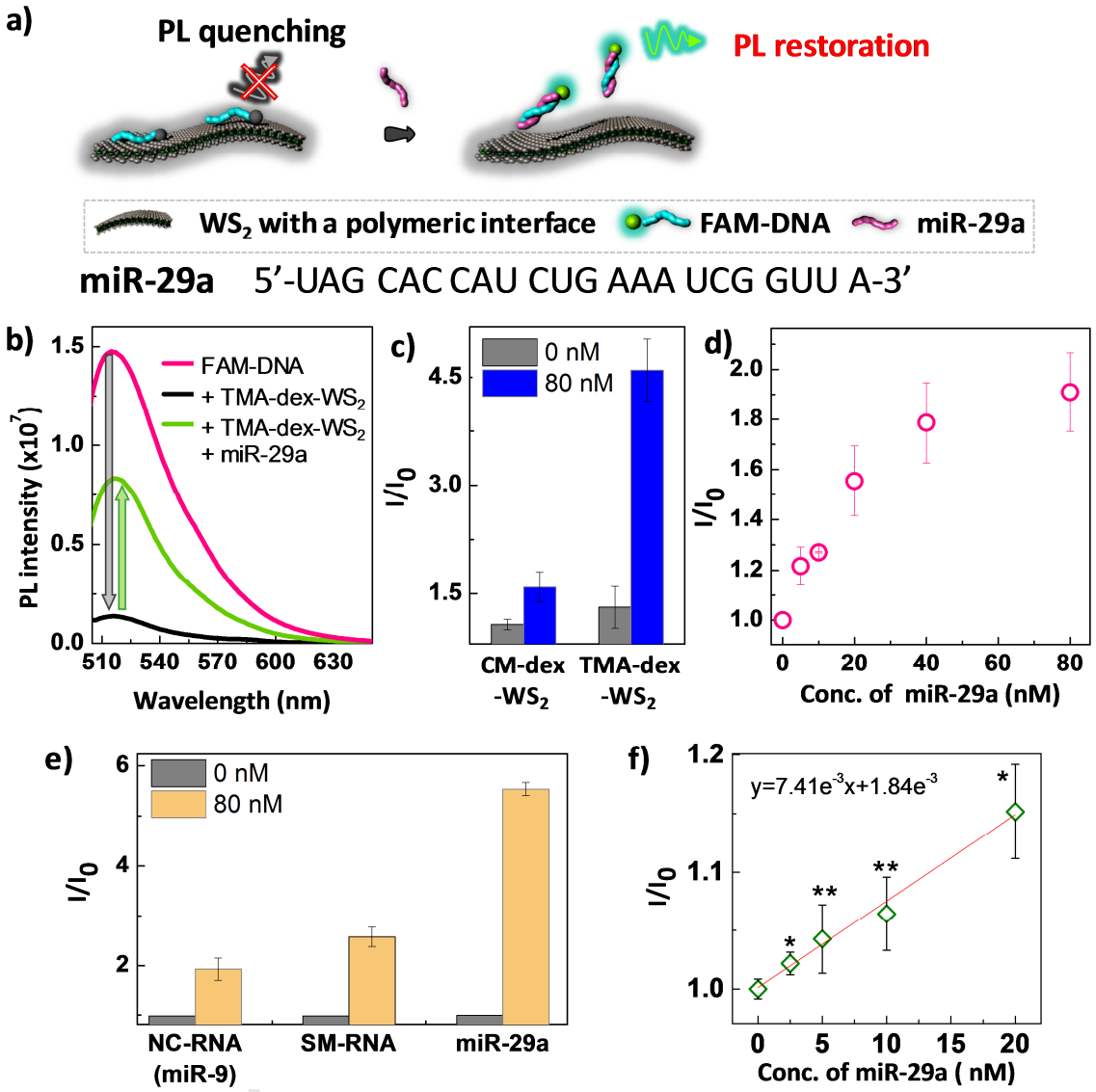

Figure 6. Detection of miR-29a in human serum. a) Schematic illustration for the detection of miR-29a on WS_2 nanosheets with different polymeric interfaces. b) PL spectra of FAM-DNA upon addition of TMA-dex-WS_2 and miR-29a. c) Restored PL intensity of FAM-DNA adsorbed on CM-dex-WS_2 or TMA-dex-WS_2 60 min after addition of miR-29a (80 nM). d) Restored PL intensity of FAM-DNA adsorbed on TMA-dex-WS_2 as a function of miR-29a concentrations. e) PL recovery responses of FAM-DNA adsorbed on TMA-dex-WS_2 to non-complimentary DNA (NC-DNA, miR-9), single base-mismatched DNA (SM-DNA), and miR-29a 30 min after incubation. f) Detection of miR-29a on TMA-dex-WS_2 adsorbing FAM-DNA in human serum. I_o and I are the fluorescence intensity of the FAM-DNA

adsorbed on the TMA-dex-WS_2 in the absence and presence of miR-29a, respectively. *P < 0.05; **P < 0.01 (n=3) using t-Test. Results are expressed as means ± SD of three experiments.

TOC Figure

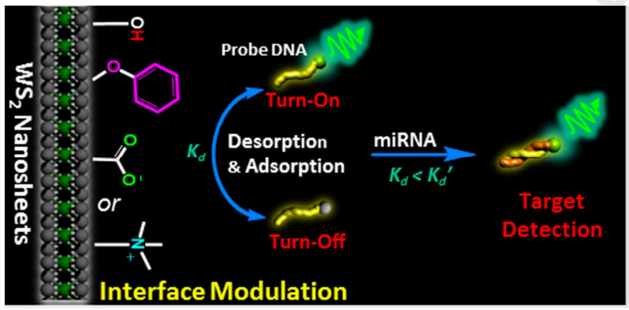

Highlights

1. The interface of WS_2 nanosheets was modulated by polymeric phases to design FRET-based biosensors.
2. DNA adsorption kinetics and thermodynamics were controlled by different polymeric phases on WS_2.
3. TMA-dex-WS_2 exhibited suitable adsorption and desorption properties for a probe DNA and miRNA.
4. A WS_2 nanosheet FRET sensor selectively detected miRNA specific for Alzheimer's disease in serum.

Graphical abstracts

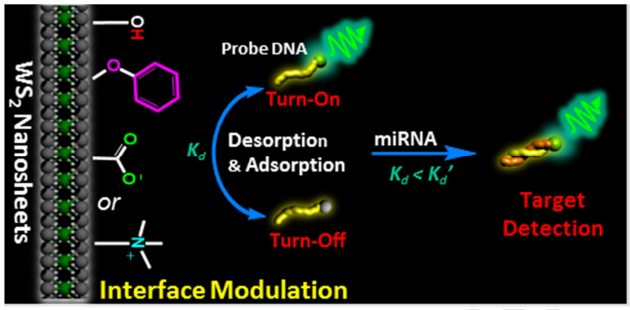

Hye-In Kim: Conceptualization, Methodology, Data Curation, Writing - original draft, Visualization, Investigation. **DaBin Yim:** Visualization, Validation, Investigation. **Su-Ji Jeon:** Investigation, Validation, Data curation. **Tae-Woog Kang:** Investigation, Investigation, Data curation. **In-Jun Hwang:** Investigation, Resources. **Sin Lee:** Investigation, Visualization. **Jin-Kyung Yang:** Methodology, Investigation, Formal analysis. **Jong-Min Ju:** Methodology, Formal analysis. **Yoon-Hee So:** Resources, **Jong-Ho Kim:** Conceptualization, Methodology, Visualization, Investigation, Writing - review & editing, Supervision.

Declaration of interests

☒ The authors declare that they have no known competing financial interests or personal relationships that could have appeared to influence the work reported in this paper.